Dipole Models for Forward/Inverse Torque Computation of a Spherical Motor

Kok-Meng Lee, *Fellow, IEEE*, Kun Bai, and Jungyoul Lim

***Abstract*—This paper presents an alternative method to model a multilayer voice coil or an air-cored electromagnet as an equivalent permanent magnet (ePM) such that its magnetic field can be characterized by a distributed set of multipoles model. We validate the ePM model by comparing the computed results against exact solutions and illustrate its effectiveness in computing the magnetic force using the dipole force equation. Unlike methods that are based on the Lorentz force equation or the Maxwell stress tensor, which require computing the volume or surface integrals to derive the forces, the closed-form dipole force method that replaces integrations with summations dramatically reduces computation time. We compare the dipole force computation against results of the Lorentz force equation and the Maxwell stress tensor method, and validate the comparisons against published experimental data. To demonstrate the effectiveness of the method, we compute the inverse torque model of a 3-DOF orientation stage operated on the principle of a spherical motor that has more controlling inputs than its mechanical DOF.**

***Index Terms*—Dipole force model, electromagnet (EM), inverse torque model, spherical actuator.**

I. Introduction

GROWING demands for miniature devices along with the trend to downscale equipment for automating the manufacture of these products on "desktops" have motivated the development of mechanically compact actuators for smooth orientation of a workpiece. One such actuator is a ball-joint-like spherical wheel motor (SWM) [1] capable of offering multi-DOF in a single joint. As shown in Fig. 1, the SWM utilizes a distributed set of electromagnets (EMs) to control the rotor consisting of high-coercive permanent magnets (PMs). The spherical motor has more controlling inputs than its mechanical DOF; the overactuating system offers an effective means to minimize energy inputs for a given torque specification.

Both forward and inverse torque models are required in the design and control of a spherical motor. The forward model simulates the magnetic torque for a given set of electrical inputs. The inverse model (required for both design analysis and real-time control) computes an optimal set of electrical inputs to deliver the specified torque. Two methods commonly used in calculating the forces between stator EMs and rotor PMs of a spherical motor [2]–[4] are the Lorentz force equation and the Maxwell stress tensor. These methods require solving the magnetic field and computing a volume or surface integral to derive the force model. As general closed-form solutions are not available, the volume or surface integrals are often solved numerically.

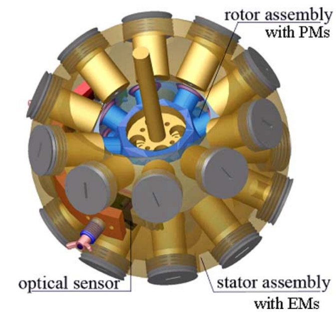

Fig. 1. SWM CAD model [1].

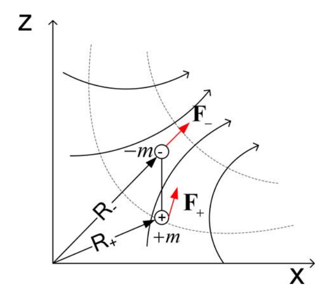

Fig. 2. Force on dipoles [6].

An alternative method is to compute the magnetic force using the Lorentz force law in analogy to that on an electric charge [5], as illustrated in Fig. 2, where we define a dipole (with strength m) as a pair of source and sink separated by a finite distance. The force $\mathbf{F}$ and torque $\mathbf{T}$ acting on the dipole can be written (in analogy to that on a stationary electric charge) [6] as

$$\mathbf{F} = \mu_0 m \left[\mathbf{H}_{R+} - \mathbf{H}_{R-}\right] \tag{1a}$$

$$\mathbf{T} = \mu_0 m \left[\mathbf{R}_{+} \times \mathbf{H}_{R+} - \mathbf{R}_{-} \times \mathbf{H}_{R-}\right] \tag{1b}$$

where μ_0 is free space permeability, $\mathbf{H}_{R+}$ and $\mathbf{H}_{R-}$ are the magnetic field intensities acting on the magnetic source and sink of the dipole, respectively, and the subscripts R_+ and R_- are the corresponding distances from a field point. Equation (1) suggests a closed-form solution for computing magnetic forces/torques of an actuator if both PMs and EMs and their magnetic boundaries can be modeled as dipoles.

Manuscript received October 13, 2008; revised December 5, 2008. Current version published February 13, 2009. Handled by Editor P. X. Liu and recommended by Technical Editor W.-J. Kim. This work was supported in part by the Korea Institute of Machinery and Materials (KIMM), in part by the Georgia Agricultural Technology Research Program (ATRP), and in part by the U.S. Poultry & Egg Association.

The authors are with the Woodruff School of Mechanical Engineering, Georgia Institute of Technology, Atlanta, GA 30332-0405 USA (e-mail: kokmeng.lee@me.gatech.edu; kbai@gatech.edu; jlim8@mail.gatech.edu).

Color versions of one or more of the figures in this paper are available online at http://ieeexplore.ieee.org.

Digital Object Identifier 10.1109/TMECH.2008.2010935

Recently, the interest to optimize the design of task-oriented multi-DOF EM actuators has motivated us to develop alternative techniques for analyzing magnetic fields and forces. This effort has led to the method of distributed multipoles (DMP) [7] that computes the 3-D magnetic field of a PM in a closed form. Most recently, the DMP method has been extended to account for the presence of the iron boundary in [8]. Once the PMs are represented using DMP, the torque of an SWM [9] can be computed using the Lorentz force equation that requires solving a volume integral. A practical method to further lower the time needed to compute the Lorentz force is to reduce the volume integral to a surface integral; for this, a method to derive an equivalent single layer (ESL) model to approximate the magnetic field of a multilayer (ML) voice coil was proposed in [10]. While the ESL model is time-efficient for calculating Lorentz forces, the modeling error, however, increases with coil thickness, particularly within the core. For applications where compact coil designs play an important role to achieve high torque-to-volume ratios, a more accurate yet efficient analytical solution for predicting the magnetic field and force of an EM is desired.

Here, we offer an improved method to derive an equivalent PM (ePM) such that the magnetic field of the original ML EM can be characterized by DMP [7]. This method (which derives an ePM for an ML EM) complements the procedure discussed in [9], where focuses have been on the modeling of PMs to analyze their effects on the forward torque model. With both the PMs and EMs modeled as DMP, the magnetic forces on the system can be calculated using the Maxwell stress tensor method or the dipole force equation. Unlike the commonly used Lorentz force equation and the Maxwell stress tensor method, the dipole force equation (replacing integrations with summations) dramatically reduces computation time. As will be shown, the closed-form dipole model is an efficient way to compute the inverse torque model of an overactuated system, especially for wrist-like spherical motors [9] where a large number of stator EMs and PMs are involved.

The remainder of this paper offers the following.

1) We illustrate the procedure of modeling an ML EM as an ePM so that its magnetic field can be characterized by a distributed set of multipoles (DMP). We validate the DMP model derived for a cylindrical ML coil by comparing the computed magnetic fields against known solutions [11]. The discussion offers intuitive insight to the effects of key design parameters on the magnetic flux.
2) With PMs and EMs in a system modeled as DMP, we derive the magnetic forces between EMs and PMs in a system using the dipole force equation. We compare the dipole force computation against results obtained using the Lorentz force equation and the Maxwell stress tensor method, and validate the comparisons against published experimental data [12], [13].
3) Finally, we demonstrate the effectiveness of the ePM method and dipole force equation for solving the inverse torque model of a 3-DOF orientation stage operated on the principle of a spherical motor.

While describing in the context of an SWM, the dipole method can be applied to other PM-based spherical motors [14]–[16] and their applications [17], [18] for modeling the nonferrous EMs and for computation of magnetic fields.

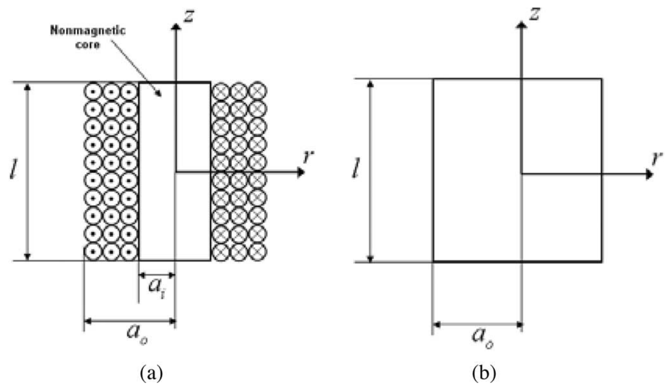

Fig. 3. (a) ML EM. (b) ePM.

II. DMP Model of an ML EM

The process of modeling an ML EM as an ePM involves finding an equivalent magnetization $\mathbf{M}$ in terms of the current density $\mathbf{J}$ and geometry of the EM. The magnetic flux density created at $\mathbf{R}'(x', y', z')$ to the field point $\mathbf{R}(x, y, z)$ is given by the Biot–Savart law [11]

$$\mathbf{B}_{\mathrm{EM}} = \frac{\mu_0}{4\pi}\int_V \frac{\mathbf{J}\times(\mathbf{R}-\mathbf{R}')}{|\mathbf{R}-\mathbf{R}'|^3}dV \tag{2a}$$

where μ_0 is the free space permeability. For a PM, the magnetic flux density can be calculated from the negative gradient of the analytical magnetic potential [11]

$$\mathbf{B}_{\mathrm{PM}} = \frac{\mu_0}{4\pi}\int_V \frac{-(\nabla\cdot\mathbf{M})(\mathbf{R}-\mathbf{R}')}{|\mathbf{R}-\mathbf{R}'|^3}dV + \frac{\mu_0}{4\pi}\int_S \frac{(\mathbf{M}\cdot\mathbf{n})(\mathbf{R}-\mathbf{R}')}{|\mathbf{R}-\mathbf{R}'|^3}dS \tag{2b}$$

where $\mathbf{n}$ is the unit surface normal. Unlike (2a), the calculation of $\mathbf{B}_{\mathrm{PM}}$ does not need the cross product of $\mathbf{J}$ and $\mathbf{R}-\mathbf{R}'$ vectors. Equations (2a) and (2b) provide the basis for deriving an ePM for the ML EM. The interest here is to seek the field solution outside the physical region of the EM, particularly near its boundary along the magnetization axis.

The procedure for deriving the ePM is best illustrated through an example. Cylindrical PMs and EMs are commonly used. Some analytical and experimental results are also available for model validation. They are used here for clarity to illustrate the DMP modeling procedure.

A. Cylindrical EM

Fig. 3(a) and (b) shows the geometry of the cylindrical EM and its corresponding ePM (with the same l and a_o). The current density of the EM is given by

$$\mathbf{J} = J(r)\mathbf{e}_\theta, \qquad \text{where } \begin{cases} J(r) = 0, & 0 \le r < a_i \\ J(r) = J, & a_i \le r \le a_o \end{cases} \tag{3}$$

and a_i and a_o are the inner and outer coil radii.

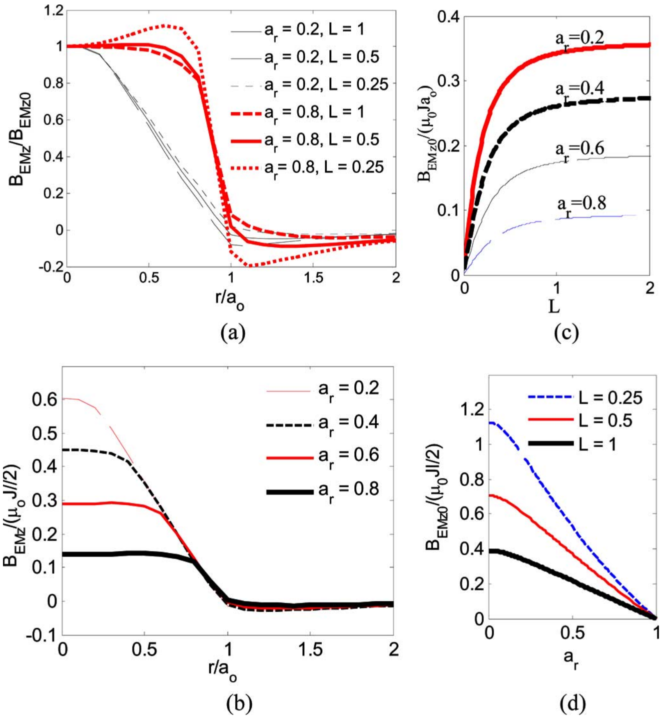

Fig. 4. Effect of a_r and L on $B_{\mathrm{EM}z0}(\varepsilon/l = 0.01)$. (a) Radial distribution of $B_{\mathrm{EM}z}$. (b) Effect of a_r ($L = 0.5$). (c) Effect of L. (d) Effect of a_r.

From (2a), the z-component of the EM flux density can be calculated

$$\frac{B_{\mathrm{EM}z}(X,Y,Z)}{\mu_0 J\,(l/2)} = \frac{1}{4\pi}\int_{a_r}^{1}\int_{-1}^{1}\int_{0}^{2\pi} \times \frac{\rho\,(\rho - X\cos\theta - Y\sin\theta)\,d\theta\,dZ'\,d\rho}{[(X-\rho\cos\theta)^2 + (Y-\rho\sin\theta)^2 + L^2(Z-Z')^2]^{3/2}} \tag{4}$$

where $(X,Y,Z) = (x/a_o, y/a_o, 2z/l)$, $\rho = r/a_o$, $a_r = a_i/a_o$, and $L = l/(2a_o)$. A general closed-form solution to (4) is not available. To investigate the effect of the aspect ratios (a_r and L) on $B_{\mathrm{EM}z}$ for actuator design, we numerically integrate (4) at $z = l/2 + \varepsilon$ along the radial direction, where ε is a positive number. The results are graphed in Fig. 4. In Fig. 4(a), the values are normalized to $B_{\mathrm{EM}z0}$, or to the value of $B_{\mathrm{EM}z}$ at $(0, 0, Z = 1 + 2\varepsilon/l)$, given in

$$\frac{B_{\mathrm{EM}z0}}{\mu_0 J a_o} = L\ln\left(\frac{1+\rho_{o-}}{a_r+\rho_{i-}}\right) + L\left(\frac{\varepsilon}{l}\right)\ln\left[\frac{(1+\rho_{o-})(a_r+\rho_{i+})}{(1+\rho_{o+})(a_r+\rho_{i-})}\right] \tag{5}$$

where $\rho_{o+} = \sqrt{4L^2\,(\varepsilon/l)^2 + 1}$, $\rho_{o-} = \sqrt{4L^2\,(1+\varepsilon/l)^2 + 1}$, $\rho_{i+} = \sqrt{4L^2\,(\varepsilon/l)^2 + a_r^2}$, and $\rho_{i-} = \sqrt{4L^2\,(1+\varepsilon/l)^2 + a_r^2}$.

When $\varepsilon/l \ll 1$ or near the physical boundary

$$\left.\frac{B_{\mathrm{EM}z0}}{\mu_0 Jl/2}\right|_{(\varepsilon/l)\to 0} = \ln\left(\frac{1+\sqrt{1+4L^2}}{a_r+\sqrt{a_r^2+4L^2}}\right). \tag{5a}$$

Some observations can be made in Fig. 4.

1) As shown in Fig. 4(a) and (b), $B_{\mathrm{EM}z}$ linearly decreases from a_i to a_o along the radial direction. When $0.25 \le L \le 1$, $B_{\mathrm{EM}z}$ is relatively uniform inside the air core. $B_{\mathrm{EM}z0}$ increases with coil thickness (or smaller a_r) for the same a_o and l, implying that thicker coils have higher magnetic fluxes (proportional to the area under the curve).
2) Fig. 4(c) shows that the drop in $B_{\mathrm{EM}z0}$ is approximately linear with a_r. $B_{\mathrm{EM}z0}$, however, increases exponentially with L and approaches a constant for a given a_r [see Fig. 4(d)].

B. Equivalent Magnetization $\mathbf{M}$ of the ePM

For a cylindrical PM, $\mathbf{M}$ is zero outside the physical boundary where $r \ge a_o$. This and the aforementioned observations suggest that the magnetization of the ePM takes the form

$$\mathbf{M} = M(r)\mathbf{e_z}, \quad \text{where} \begin{cases} M(r) = M_o, & 0 \le r < a_i \\ M(r) = M_o - J(r - a_i), & a_i \le r \le a_o \end{cases} \tag{6}$$

where M_0 is an integral constant to be found by comparing (2a) and (2b). Since the flux density of the cylindrical ePM has a maximum along its magnetization, we find M_0 from $B_{\mathrm{PM}z} = B_{\mathrm{EM}z}$ at $(0, 0,\ l/2 + \varepsilon)$. Substituting (6) into (2b) and noting that $\nabla\cdot\mathbf{M} = 0$, the first term on the right-hand side of (3) disappears and the second term can be written as

$$\frac{B_{\mathrm{PM}z0}}{\mu_0 Jl/2} = \frac{B_{\mathrm{EM}z0}}{\mu_0 Jl/2} + \frac{1}{Jl}\left[J\,(a_o - a_i) - M_0\right]\left(\frac{\varepsilon}{\rho_{o+}a_o} - \frac{l+\varepsilon}{\rho_{o-}a_o}\right) \tag{7}$$

where M_0 can now be determined by equating the last term of (7) to zero such that $B_{\mathrm{PM}z0} = B_{\mathrm{EM}z0}$. As the factor involving the independent variable ε is not always zero, $M(r) = J(a_o - a_i)$. Hence, the equivalent magnetization $\mathbf{M}$ graphically illustrated in Fig. 5(a) is given by

$$\mathbf{M} = M(r)\mathbf{e_z}, \quad \text{where} \begin{cases} M(r) = J(a_o - a_i), & 0 \le r < a_i \\ M(r) = J(a_o - r), & a_i \le r \le a_o. \end{cases} \tag{8}$$

C. Dipole Model of an ML EM (DMP_{EM})

Once the ePM is found, the EM can be modeled using a DMP [7]. For a cylindrical PM, the DMP consists of k circular loops of n equally spaced dipoles parallel to the magnetization vector, as shown in Fig. 5(b). The loops (each with radius $\bar{a}_j$) are uniformly spaced

$$\bar{a}_j = \frac{a_o j}{k+1}, \qquad \text{at } z = \pm\frac{\bar{\ell}}{2} \tag{9}$$

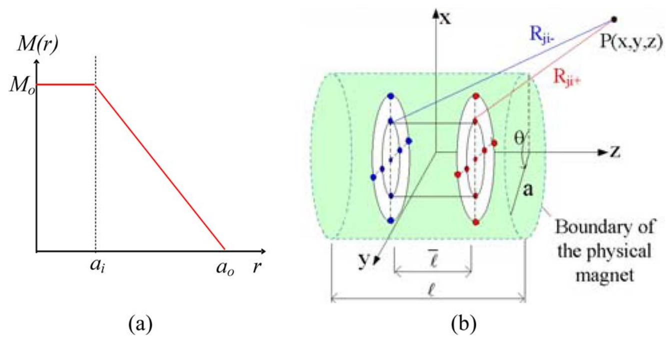

Fig. 5. DMP model of a magnet. (a) Equivalent $\mathbf{M}$. (b) Dipole distribution.

TABLE I
SIMULATION PARAMETERS

1000turns, 28 AWG, 1A Current
ML: a_o =15.88mm, a_r=0.3, L=0.3
ESL: $J_e d_w$=120.1A/mm, a_e=12mm
DMP$_{EM}$: n=16, k=6, $\bar{l}\,/\,l$ = 0.442
m_i (μA/m): 1.476, 0.547, 1.618, 1.644, 1.654, 1.325, 0.592

where $0 \le j \le k$. The flux density at point $\mathbf{P}(x, y, z)$ can be computed using

$$\mathbf{B} = \frac{\mu_0}{4\pi} \sum_{i=0}^{k} m_i \sum_{j=1}^{n} \left(\frac{\mathbf{R}_{ij+}}{|\mathbf{R}_{ij+}|^3} - \frac{\mathbf{R}_{ij-}}{|\mathbf{R}_{ij-}|^3} \right) \tag{10}$$

where $\mathbf{R}_{ij+}$ and $\mathbf{R}_{ij\_}$ are the vectors from the source and sink of the jth dipole on the ith loop to $\mathbf{P}$, respectively. The procedure of deriving the parameters (k, n, $\bar{\ell}$, and m_i) of the DMP for a cylindrical PM can be found in [7].

III. MODEL VALIDATION

We validate the DMP derived for a circular EM by comparing the magnetic field distribution and force computation against known solutions. The results are given in Section III-A and III-B, followed by discussions in Section III-C.

A. Validation of Magnetic Field Computation

As a basis for model validation, we numerically integrate the exact integral equation (4) for the flux density of an ML EM so that the DMP$_{\mathrm{EM}}$ model and the ESL approximation can be compared. Table I lists the dimensions of the EM and the values of the parameters defining the ESL and DMP$_{\mathrm{EM}}$ models. Since the ESL model is singular at the surface, we plot B_z and B_r along the radial direction at $z = l/2 + \varepsilon$, with $\varepsilon = 0.55$ mm, and B_z along the z-axis for the thick EM in Fig. 6.

B. Validation of Magnetic Force Computation

We compute the magnetic force between an PM and an EM for two test setups shown in Fig. 7. Published experimental force data [12] (numerically validated with a mesh-free method in [13]) are available for comparison. In the following computation, the PMs are modeled as DMP$_{\mathrm{PM}}$ [7], with the parameters summarized in Table II.

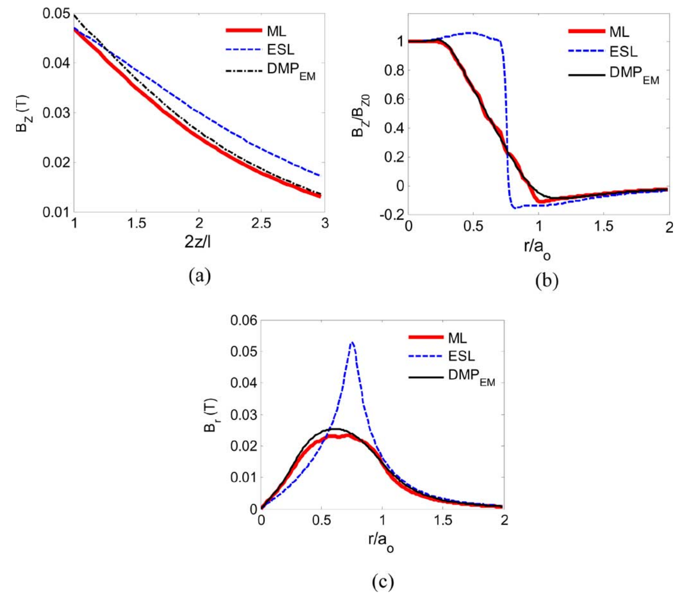

Fig. 6. $B_{\mathrm{EM}\,z}$ and B_r in tesla (EM1). (a) B_z along the z-axis. (b) B_z at $\varepsilon = 0.55$ mm. (c) B_r at $\varepsilon = 0.55$ mm.

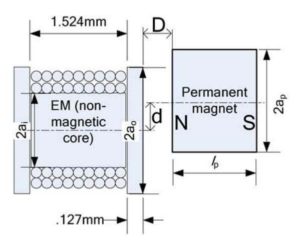

Size	Large	Small
a_o (mm)	1.981	0.767
a_r	0.7693	0.48
L	0.385	0.48
Coil res. (Ω)	57	32
Wire length (m)	3	1.68
Coil: 280 turns of #47 wire; Current=0.05A		
a_p (mm)	1.499	0.8
L_p	0.533	0.508
Samarium-Cobalt magnet; $\mu_0 M_0$=1.02 T		

Fig. 7. Experimental setup [12] and parameters.

TABLE II
VALIDATION SIMULATION PARAMETERS

	Parameters	Large	Small
PM DMP$_{PM}$	**n, k,** $\bar{l}\,/\,l$	6, 2, 0.314	6, 2, 0.3122
	m_i (μA/m)	1.65, 0.02, 3.8	0.43, 0.02, 1.07
EM (ESL)	$J_e d_w$ (μA/mm)	22.75	38.98
	a_e (mm)	1.8168	1.456
EM (DMP$_{EM}$)	n, k, $\bar{l}\,/\,l$	12, 8, 0.7661	8, 3, 0.7441
	m_i (nA/m)	0.236, 0.177, 0.366, 0.567, 0.751, 0.914, 1.032, 1.28, 0.312	1.354, 1.758, 3.32, 1.661

Three different methods for modeling the magnetic fields and forces are compared.

Method I computes the force using Maxwell stress tensor

$$\mathbf{F} = \oint_C \mathbf{T}\, dC, \quad \text{where } \mathbf{T} = \frac{1}{\mu_0}\left(\mathbf{B}(\mathbf{B}\cdot\mathbf{n}) - \frac{1}{2}B^2\mathbf{n}\right) \tag{11}$$

where C is an arbitrary boundary enclosing the body of interest and $\mathbf{n}$ is the normal of the boundary interface. Equation (11) requires the total field $\mathbf{B}$ (contributed by both the PM and EM) to compute the force by the surface integration. As a basis for comparison, the $\mathbf{B}$-field of the ML EM is numerically computed using (2a).

Method II calculates the Lorentz force exerted on the current carrying EM

$$\mathbf{F} = -\oint \mathbf{B} \times I\, d\mathbf{n}, \qquad \text{where } I = \oiint J\, dS \tag{12}$$

where $\mathbf{n}$ is the unit current direction vector and S is the cross section of wire. Since the current density vector $\mathbf{J}$ is directly used in the calculation, only the $\mathbf{B}$-field of the PM is needed in the Lorenz force equation (12). The ML EM is replaced with the ESL model [7] (with equivalent current density J_e, wire diameter d_w, and coil radius a_e), which reduces the volume integral to a surface integral.

Method III used the dipole force equation in analogy to that on a stationary electric charge by the Lorentz law [5] to compute the net force acting on the PM

The net force is simply the summation of the individual forces on the dipoles that characterize the PM

$$\mathbf{F} = \frac{\mu_0}{4\pi} \sum_{i=1}^{n_r} m_{r_i} \sum_{j=1}^{n_s} m_{s_j} (\mathbf{R}_{s_{j+}r_{i+}} - \mathbf{R}_{s_{j+}r_{i-}} + \mathbf{R}_{s_{j-}r_{i-}} - \mathbf{R}_{s_{j-}r_{i+}}). \tag{13}$$

In (11), $\mathbf{R}_{s_\pm r_\pm} = (\mathbf{R}_{s\pm} - \mathbf{R}_{r\pm}) \,/\, |\mathbf{R}_{s\pm} - \mathbf{R}_{r\pm}|^3$, and n_r and n_s are the number of dipoles of the PM and EM, respectively. The EM is modeled as $\mathrm{DMP_{EM}}$.

The parameters for the ESL model and the $\mathrm{DMP_{EM}}$ are summarized in Table II. The magnetic fields of the large and small coils are given in the left and right columns in Fig. 8, where B_z is plotted along the z-axis, and B_z and B_r are plotted along the radial direction at $z = l/2 + \varepsilon$, with $\varepsilon = 0.55$ mm. The computed forces F are compared against published experimental data F_{exp} in Fig. 9. Table III compares the time required to compute 26 data points in Fig. 9(a) using a computer with Quad Core 2.66 GHz CPU and 8 GB RAM.

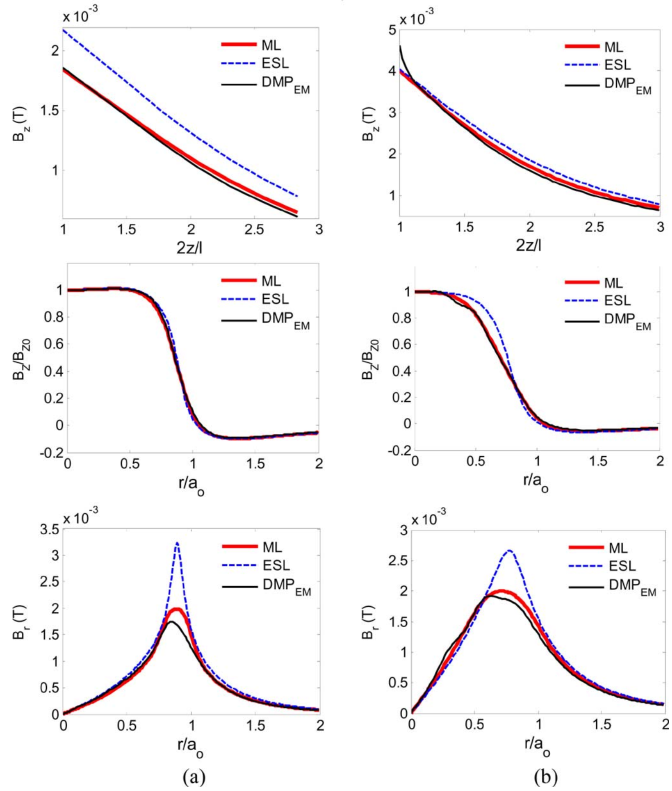

Fig. 8. Computed magnetic flux density. (a) Large. (b) Small.

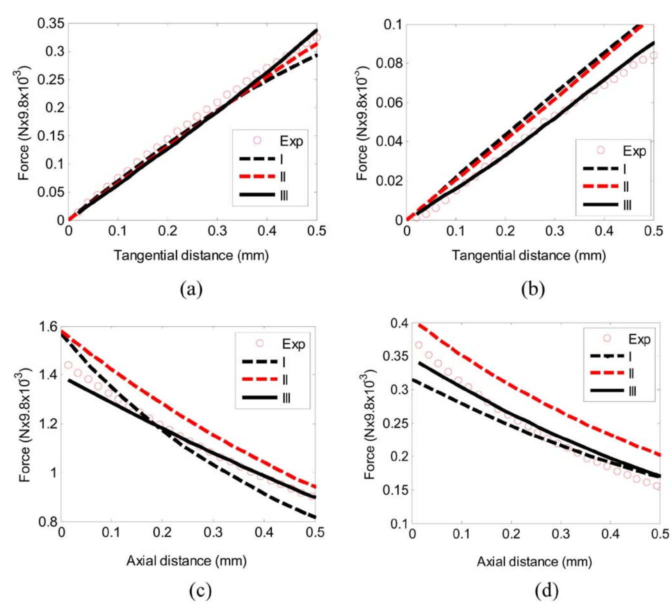

Fig. 9. Computed forces and experimental data. (a) Tangential force, large coil. (b) Tangential force, small coil. (c) Axial force, large coil. (d) Axial force, small coil.

C. Discussion of Results

Some observations in Figs. 6, 8, and 9, and Table III are discussed as follows.

1) Unlike the ESL model where the equivalent current density J_e is determined from the 2-D magnetic field, the equivalent magnetization $\mathbf{M}$ of the ePM is derived using the complete 3-D integral. As shown in Figs. 6 and 8, the $\mathrm{DMP_{EM}}$-modeled flux densities agree very well with the solutions to the exact integral equation (4) for both thin and thick coils. The ESL model provides a reasonable prediction of the z-component flux density, but discrepancies from the exact solutions increase with coil thickness (or smaller a_i/a_o).

2) The Maxwell stress tensor in method I can be computed using the $\mathrm{DMP_{PM}}$ and $\mathrm{DMP_{EM}}$, which yields the same solution to the dipole force equation as in method III. However, unlike the Maxwell stress tensor method or the Lorentz force equation (with the ESL approximation) that require numerical computations of a surface integration, the dipole force equation (replacing integrations with

TABLE III
COMPARISON OF COMPUTATION TIME

Method	**I**	**II**	**III**
Computation Time (sec)	106.03	21.53	0.0625

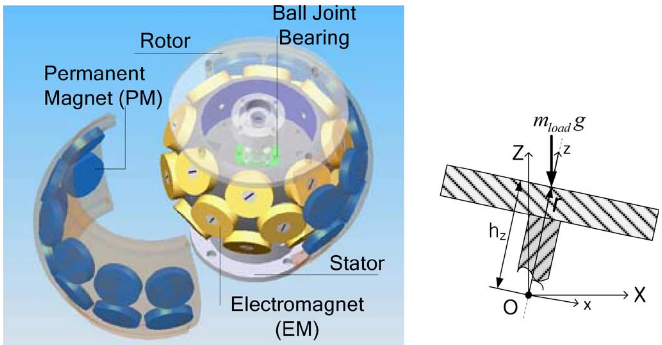

(a) (b)

Fig. 10. 3-DOF orientation stage. (a) CAD model. (b) Table and load.

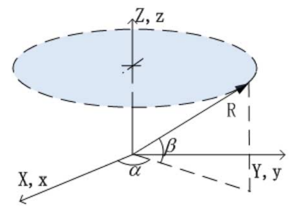

Stator EM locations		
EM$_j$	β_s(deg)	α_s(deg)
1 to 8	26	45(j–1)
9 to16	–26	45(j–9)
17 to 24	0	45(j–17)+22.5
Rotor PM locations		
PM$_i$	β_r(deg)	α_r(deg)
1 to 12	15	30(i-1)
13 to 24	–15	30(i-13)

Fig. 11. Parameters defining the pole locations.

TABLE IV
CURRENT LAYOUT OF THE EMS

$I_1=I_{13}=u_1$	$I_5=I_9=u_5$	$I_{18}=I_{19}=-I_{22}=-I_{23}=u_9$
$I_2=I_{14}=u_2$	$I_6=I_{10}=u_6$	$I_{17}=-I_{20}=-I_{21}=I_{24}=u_{10}$
$I_3=I_{15}=u_3$	$I_7=I_{11}=u_7$	
$I_4=I_{16}=u_4$	$I_8=I_{12}=u_8$	

summations) is in closed form, dramatically reducing computation to 0.0625 s, as shown in Table III.

3) As shown in Fig. 9, the Maxwell stress tensor and the dipole force equation (or methods I and III, respectively) agree very closely with published experimental data while the ESL model (which reduces the volume integral of the ML EM to a surface integral of a single-layer coil) overestimates the computed forces as expected.

IV. ILLUSTRATIVE 3-DOF ORIENTATION STAGE

With EMs and PMs modeled as DMP, the dipole force model is an efficient way to compute the magnetic force in 3-D space for the design of an EM system, especially for wrist-like spherical motors [9] involving a large number of EMs and PMs. As an illustrative example, Fig. 10 shows the computer-aided design (CAD) model of an (ball-joint-like) orientation stage operated on the principle of an SWM [1]. Unlike the SWM (Fig. 1) where the rotor PMs are embedded in the "ball," the PMs of the 3-DOF stage in Fig. 10(a) are housed in the socket-like rotor assembly. In Fig. 10(a), the stator EMs are air-cored and the structure (except PMs) is nonmagnetic. Supported on a bearing, the rotor is concentric with the stator; thus, the system has 3 DOF. The rotor of the 3-DOF orientation stage is subjected to an external torque T_{ext} in Fig. 10(b), where the center of gravity coincides with the rotation center

$$T_{\text{ext}} = r \times m_{\text{load}}\,g. \tag{14}$$

Statically, the torque acting on the rotor is equal to the external torque. The interest here is to simulate the maximum current inputs required for meeting a torque specification over the operating range

$$0 \le (\psi, \phi) \le 360^\circ \qquad \text{and} \qquad -22.5 \le \theta \le 22.5^\circ$$

where (ψ, θ, ϕ) are the *ZYZ* Euler angles of the rotor.

As shown in Fig. 10(a), the PMs and EMs are equally spaced on layers of circular planes with their radial magnetization axes passing through the motor center. The magnetization axes are characterized mathematically by vectors in terms of the two angles (α from the x-axis to the projection on the *xy*-plane, and β from the *xy*-plane to the vector as defined in Fig. 11). The magnetization vector of the ith PM is given in rotor coordinates (x, y, z) by (15)

$$\mathbf{r}_i = (-1)^{i-1}\left[\cos\beta_{ri}\cos\alpha_{ri} \quad \cos\beta_r\sin\alpha_{ri} \quad \sin\beta_{ri}\right]^{\mathrm{T}}. \tag{15}$$

Similarly, the jth EM magnetization (in stator frame *XYZ*) is

$$\mathbf{s}_j = \left[\cos\beta_{sj}\cos\alpha_{sj} \quad \cos\beta_{sj}\sin\alpha_{sj} \quad \sin\beta_{sj}\right]^{\mathrm{T}}. \tag{16}$$

In (15) and (16), the subscripts "r" and "s" denote the rotor and stator, respectively. Unlike the PM, the direction of the EM is defined by the polarity of the current. The orientation stage (Fig. 10) has three layers of eight stator EMs and two layers of 12 rotor PMs; the coordinates are given in Fig. 11. The PMs and EMs are arranged in pairs such that they are electromechanically symmetric. Because of the symmetry, the EMs are grouped into ten electrical inputs (Table IV). Unlike the SWM (Fig. 1), the orientation stage (Fig. 10) has a third layer of EMs (EM17–EM20) along the equator offering additional torques about the *xy*-plane.

A. Forward Torque Model

The forward torque model of the PM-based spherical motor with linear magnetic properties has the form [3], [9]

$$\mathbf{T} = \left[T_X \quad T_Y \quad T_Z\right]^{\mathrm{T}} = \left[\bar{\mathbf{K}}\right]\mathbf{I} \tag{17}$$

where

$$\bar{\mathbf{K}}(\in \mathbb{R}^{3\times m_s}) = \left[\vec{K}_1 \quad \cdots \quad \vec{K}_p \quad \cdots \quad \vec{K}_{m_s}\right] \tag{17a}$$

$$\mathbf{I} = \left[I_1 \quad \cdots \quad I_p \quad \cdots \quad I_{m_s}\right]^{\mathrm{T}} \tag{17b}$$

where I_p is the current input to the pth EM and m_s is the total number of EMs. In (17a), the torque characteristic vector ($\vec{K}_p \in \mathbb{R}^{3\times 1}$, contributed by I_p to the whole rotor) at each orientation (ψ, θ, ϕ) can be derived using the dipole force equation

$$\vec{K}_p = \frac{\mu_0}{4\pi}\sum_{i=1}^{n_r} m_{r_i} \sum_{j=1}^{n_p} m_{s_j}\left[(\mathbf{R}_{s_{j+}r_{i+}} - \mathbf{R}_{s_{j-}r_{i+}}) \times \mathbf{R}_{r_{i+}} - (\mathbf{R}_{s_{j+}r_{i-}} - \mathbf{R}_{s_{j-}r_{i-}}) \times \mathbf{R}_{r_{i-}}\right] \quad (18)$$

where n_p (or n_r) is the number of dipoles for each EM (or PM).

B. Inverse Torque Model

Since the 3-DOF orientation stage has more current inputs than its mechanical DOF, the optimal current input vector for a given torque is found by minimizing the input energy consumption subject to the required torque constraint. Provided that the input currents are kept within limits, the optimal current input vector can be solved using Lagrange multipliers. For a system where m_s EMs are grouped into m independent inputs, the optimal solution for $\mathbf{u} = [\,u_1 \quad \cdots \quad u_p \quad \cdots \quad u_m\,]^{\mathrm{T}}$ can be written in closed form [3]

$$\mathbf{u} = [\mathbf{K}]^{\mathrm{T}}([\mathbf{K}][\mathbf{K}]^{\mathrm{T}})^{-1}\mathbf{T}. \quad (19)$$

For the layout in Table IV where $m = 10$, and thus, $\mathbf{K}(\in \mathbb{R}^{3\times 10})$

$$\mathbf{K} = [(\vec{K}_1 + \vec{K}_{13}) \quad (\vec{K}_2 + \vec{K}_{14}) \quad \cdots \quad (\vec{K}_{17} - \vec{K}_{20} - \vec{K}_{21} + \vec{K}_{24})]. \quad (19a)$$

C. Simulation Results

Two sets of simulation results are given here to illustrate the effects of pole sizes on the magnetic torque and the inverse torque model of the orientation stage.

1) Effect of Pole Size on the Magnetic Torque: Observations in Fig. 4 suggest that both small a_r and L (for a given a_o) have a significant effect on the increase in the z-component magnetic fluxes, and hence, on the compact design of a spherical motor. The effect can be illustrated with the example in Fig. 12 and Table V, where two pole sizes of a spherical motor are compared.

Design 1 (D1) simulates the torque between the rotor PM and stator EM of the SWM [9], where $L \geq 1$, while design 2 (D2) models that of the 3-DOF orientation stage (Fig. 10) with the same outer radius $R_o = 76.2$ mm. In D2, both the PM and EM have a much smaller L of 0.2 and 0.3, respectively, and as a result, the rotor PM (embedded in the "socket") has a 1.4 times larger rotational radius than that of D1. The EM in Table I is used for D2 and repeated here for ease of comparison.

The effects of the pole size on the magnetic torque are compared in Fig. 13 that plots the torque as a function of γ (the separation angle between the magnetzation axes of PM and EM). As compared to D1 in Fig. 13, D2 offers 2.4 times higher maximum torque and converts 3.6 times more mechanical energy (represented by the area under the torque–displacement curve).

TABLE V
PARAMETERS USED FOR STATOR AND ROTOR POLES

Design 1 (D1) [9]	**Design 2 (D2)**
$R_i = 37.5$mm	$R_i = 52.75$mm
PM: a_o =6.35mm, L=1, $\mu_o M_o$=1.27T DMP$_{PM}$: $n = 2,\ k = 6,\ \bar{l}\,/\,l = 0.7519$ m_i (μA/m): 10.64, 1.68, 37.7	PM: a_o =15.875mm, L=0.2, $\mu_o M_o$=1.31T DMP$_{PM}$: $n = 10,\ k = 4,\ \bar{l}\,/\,l = 0.3$ m_i(μA/m): 33.5, 24.5, 57.6, 52.0, 276.1
EM: a_o=9.53mm, a_r=0.5, L=1.33, # of turns =1050 DMP$_{EM}$: $n = 12,\ k = 4,\ \bar{l}\,/\,l = 0.807$ m_i (μA/m): -0.152, 0.448, 0.395, 0.515, 0.0563	EM: a_o =15.88mm, a_r=0.3, L=0.3, # of turns =1000 DMP$_{EM}$: n=16, k=6, $\bar{l}\,/\,l = 0.442$ m_i(μA/m): 1.476, 0.547, 1.618, 1.644, 1.654, 1.325, 0.592

Common parameters: 28 AWG; I = 1 A; gap = 0.5 mm; R_o = 76.2 mm.

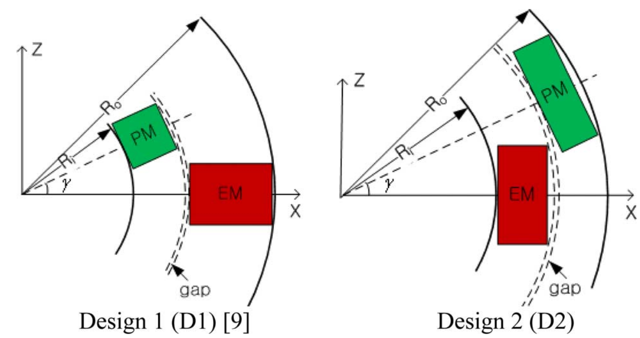

Fig. 12. Comparison of design parameters ($R_o = 76.2$ mm).

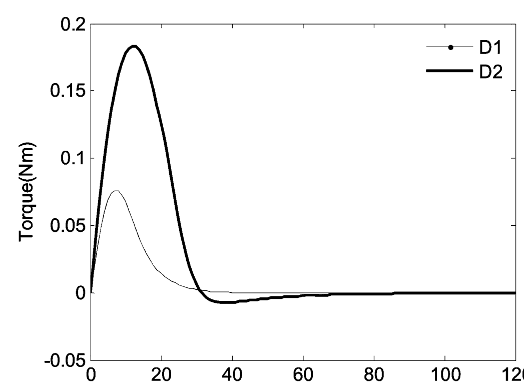

Fig. 13. Effect of pole geometries on actuator torque.

2) Inverse Torque Model of the Orientation Stage (D2): The parameters used in simulating the inverse torque model (19) with the component $\vec{K}_p$ given by (18) are based on Fig. 11, D2 in Table V, and Table VI. Due to symmetry, only the input profiles in the range of $0 \leq \psi \leq 90°$ and $-22.5° \leq \theta \leq 22.5°$ are plotted. Fig. 14 shows the current profiles of each of the current inputs required to maintain the external torque;

TABLE VI
ORIENTATION-STAGE SIMULATION PARAMETERS

$\mathbf{m_{load}}$ (kg)	$\mathbf{h_z}$ (mm)	**Mass** (kg)	**Moment of inertia** (kg-m^2)
8	64.8	2.03	$I_{zz}=7.97\times10^{-3}$, $I_{xx}=I_{yy}=5.89\times10^{-3}$

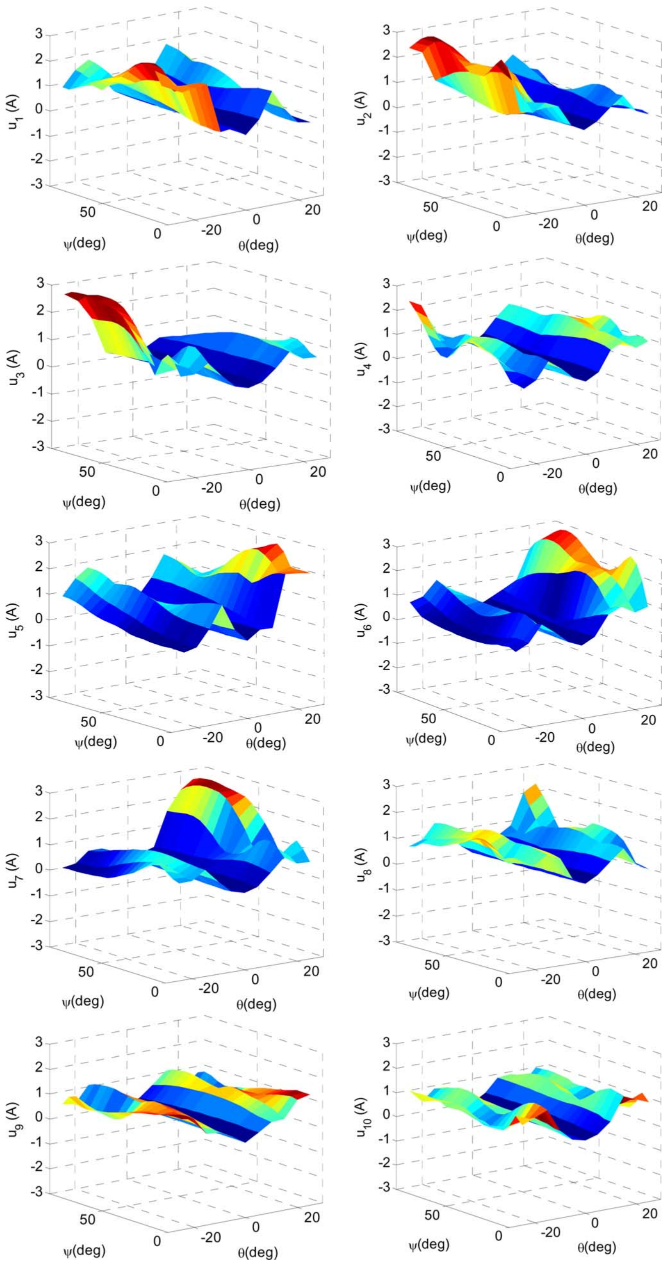

Fig. 14. Current inputs in each stator EM.

each point represents the maximum current for the orientation $(\psi,\ \theta,\ 0 \leq \phi \leq 360^{\circ})$. Except near the boundary, most of the required currents are within 2 A. The statistics of the EM-required inputs are summarized in Table VII, which suggests that the maximum current required is about 3 A for the specified load (and rotor weight) of 10 kg.

TABLE VII
INPUT STATISTICS (CURRENT IN AMPERES)

u_i (A)	**Average**	**Std. dev.**	**Max**
1	0.9163	0.7304	2.9898
2	0.8352	0.8066	3.0704
3	0.7405	0.7072	2.7797
4	0.7903	0.4872	2.2829
5	0.9163	0.7304	2.9898
6	0.8352	0.8066	3.0704
7	0.7405	0.7072	2.7797
8	0.7903	0.4872	2.2829
9	0.7256	0.4123	1.4559
10	0.6711	0.3806	1.6772

V. CONCLUSION

We have presented a new, time-efficient method for modeling an ML EM as an equivalent PM such that the magnetic field of the EM can be characterized using a DMP. The advantage of modeling the PM and EM using DMP has been illustrated through a force computation. Unlike other commonly used methods that often require to calculate a time-consuming numerical (volume or surface) integral to derive the force, the dipole model replacing integrals by summations computes magnetic forces in closed form.

The dipole models have been validated by comparing results against exact field solutions and published experimental force data, which show excellent agreement. Along with the prototype CAD design of a 3-DOF orientation stage, we simulate the maximum current inputs required of the spherical motor (150 mm $\times$ 150 mm $\times$ 150 mm) for a given design specification. The simulation suggests that the maximum current required is about 3 A for the specified load (and rotor weight) of 10 kg. Thick coils (or small a_r) with small L play an effective role to achieve high torque-to-volume ratios, and thus, are important in applications where compact coil designs are used.

Although the method has been discussed in the context of a cylindrical EM (where some analytical and experimental results are also available for model validation), it can be extended to EMs having other customized shapes.

REFERENCES

[1] K.-M. H. S. Lee and J. Joni, “Concept development and design of a spherical wheel motor (SWM),” in *Proc. IEEE ICRA*, Barcelona, Spain, Apr. 18-22, 2005, pp. 3652–3657.
[2] J. Wang, G. Jewell, and D. Howe, “Design and control of a novel spherical permanent magnet actuator with three-DOF,” *IEEE/ASME Trans. Mechatronics*, vol. 8, no. 4, pp. 457–468, Dec. 2003.
[3] Y. Liang, I. M. Chen, C. K. Lim, G. Yang, L. Wei, and K.-M. Lee, “Design and analysis of a permanent magnet spherical actuator,” *IEEE/ASME Trans. Mechatronics*, vol. 13, no. 2, pp. 238–248, Apr. 2008.
[4] K.-M. Lee, R. A. Sosseh, and Z. Wei, “Effects of the torque model on the control of a VR spherical motor,” *IFAC J. Control Eng. Pract.*, vol. 12, no. 11, pp. 1437–1449, Nov. 2004.
[5] R. M. L. J. C. Fano and R. B. Alder, *Electromagnetic Fields, Energy, and Forces*. New York: Wiley, 1960.
[6] (1998). [Online]. Available: http://web.mit.edu/6.013_book/www/chapter 11/11.8.html
[7] K.-M. Lee and H. Son, “Distributed multi-pole model for design of permanent-magnet-based actuators,” *IEEE Trans. Magn.*, vol. 43, no. 10, pp. 3904–3913, Oct. 2007.
[8] K.-M. Lee, H. Son, and K. Bai, “Image method with distributed multi-pole models for analyzing permanent-magnet-based electromagnetic actuators,” presented at the DSCC 2008, Ann Arbor, MI, Oct. 20–22.

[9] H. Son and K.-M. Lee, "Distributed multi-pole models for design and control of PM actuators and sensors," *IEEE/ASME Trans. Mechatronics*, vol. 13, no. 2, pp. 228–238, Apr. 2008.
[10] K.-M. Lee and H. Son, "Equivalent voice-coil models for real-time computation in electromagnetic actuation and sensor applications," presented at the AIM 2007, Zurich, Switzerland, Sep. 4–7.
[11] J. D. Jackson, *Classical Electrodynamics*. New York: Wiley, 1999.
[12] N. I. J. P. A. Bastos. Forces in permanent magnets. Team workshop problems 23 [Online]. Available: http://www.compumag.co.uk/team.html
[13] Q. Li and K.-M. Lee, "An adaptive meshless method for magnetic field computation," *IEEE Trans. Magn.*, vol. 42, no. 8, pp. 1996–2003, Aug. 2006.
[14] G. S. Chirikjian and D. Stein, "Kinematic design and commutation of a spherical stepper motor," *IEEE/ASME Trans. Mechatronics*, vol. 4, no. 4, pp. 342–353, Dec. 1999.
[15] M. K. Rashid and Z. A. Khalil, "Configuration design and intelligent stepping of a spherical motor in robotic joint," *J. Intell. Robot. Syst.*, vol. 40, pp. 165–181, Jun. 2004.
[16] Q. J. Wang, Z. Li, Y. Y. Ni, and W. Jiang, "Magnetic field computation of a PM spherical stepper motor using integral equation method," *IEEE Trans. Magn.*, vol. 42, no. 4, pp. 731–734, Apr. 2006.
[17] B. Ackermann, H. Steinbusch, T. Vollmer, J. Wang, G. W. Jewell, and D. Howe, "A spherical permanent magnet actuator for a high-fidelity force-feedback joystick," *IEEE/ASME Trans. Mechatronics*, vol. 14, no. 3, pp. 327–339, Apr. 2004.
[18] D. V. Lee and S. A. Velinsky, "Analysis and experimental verification of a three-dimensional noncontacting angular motion sensor," *IEEE/ASME Trans. Mechatronics*, vol. 12, no. 6, pp. 612–622, Dec. 2007.

Kok-Meng Lee (M'89–SM'02–F'05) received the B.S. degree from the State University of New York, Buffalo, in 1980, and the S.M. and Ph.D. degrees from Massachusetts Institute of Technology, Cambridge, in 1982 and 1985, respectively.

He is currently a Professor with the Woodruff School of Mechanical Engineering, Georgia Institute of Technology, Atlanta. His current research interests include system dynamics/control, robotics, automation, and mechatronics. He holds eight patents in machine vision, a 3-DOF spherical motor/encoder, and a live-bird handling system.

Prof. Lee is a Fellow of the American Society of Mechanical Engineers (ASME). He received the National Science Foundation (NSF) Presidential Young Investigator Award, the Sigma Xi Junior Faculty Research Award, the International Hall of Fame New Technology Award, and the Kayamori Best Paper Award.

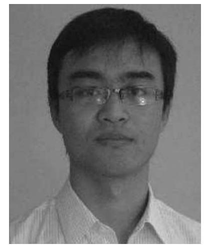

Kun Bai received the B.S. degree from Zhejiang University, Hangzhou, China, in 2006. He is currently working toward the Ph.D. degree in the Woodruff School of Mechanical Engineering, Georgia Institute of Technology, Atlanta.

His current research interests include electromagnetic actuators, sensors, system dynamics/control, and mechatronics.

Jungyoul Lim received the B.S. degree in mechanical and aerospace engineering from Seoul National University, Seoul, Korea, in 2001. He is currently working toward the Ph.D. degree in the Woodruff School of Mechanical Engineering, Georgia Institute of Technology, Atlanta.

His current research interests include electromagnetic actuators, system dynamics/control, and networking.